Available online at www.sciencedirect.com

SCIENCE DIRECT®

Journal of Sound and Vibration 279 (2005) 75–88

JOURNAL OF SOUND AND VIBRATION

www.elsevier.com/locate/jsvi

Dynamic stress concentration in a ribbed plate using the acoustical wave propagator technique

S.Z. Peng*

Centre for Acoustics, Dynamics and Vibration, School of Mechanical Engineering, The University of Western Australia, 35 Stirling HWY, Crawley, WA 6009, Australia

Received 13 May 2003; accepted 12 November 2003

Abstract

This paper presents an explicit acoustical wave propagator technique to investigate the flexural wave scattering and dynamic stress concentration in a ribbed plate based on Mindlin plate theory. A scheme combining Chebyshev polynomial expansion and fast Fourier transformation is introduced to implement the operation of the acoustical wave propagator. The exact analytical solutions are also presented to demonstrate the validity of the present technique. The wave propagation patterns are used to investigate the effect of rib on the flexural wave scattering and distribution of dynamic stress concentration. Dynamic stress concentration factors around the discontinuities are examined in detail.

1. Introduction

Structures consisting of thin plates stiffened by multiple ribs are of considerable importance in air/space and maritime industries. Due to the structural discontinuities, dynamic stress concentrations are often located near or at these rib–plate interconnections. However, although much numerical work has been done to investigate the vibration of stiffened plates, only a handful of researchers have investigated dynamic stress concentration of ribbed plates. Mukherjee and Mukhopadhyay [1] have provided a literature review, in which they have given a general picture of research on dynamic stress concentration. Other researchers have written detailed papers of particular aspects of dynamic stress concentration. Ungar [2] investigated the transmission of plate flexural waves through reinforcing ribs and discussed the dynamic stress concentration factors. Later, Stearn [3,4] examined the local increase of dynamic stress and strain in a flat plate

---

*Tel.: +61-8-9380-1901; fax: +61-8-9380-1024.
E-mail address: speng@mech.uwa.edu.au (S.Z. Peng).

0022-460X/$ - see front matter
doi:10.1016/j.jsv.2003.11.016

at a sharp change of section by the diffuse field bending wave model in the frequency domain. The spatial variation of stress, strain and acceleration in structures subject to broad frequency band excitation was also investigated. However, the effects of this kind of discontinuity on the flexural wave propagation and scattering, and the distribution of dynamic stress concentration in the time domain are not well understood. Hence, it is still necessary to develop an effective and accurate method to investigate a range of such interesting acoustical problems as dynamic stress concentration and pre-fatigue at structural discontinuities, and transient energy exchange across the coupling boundaries.

Recently, Pan and Wang [5] extended the work by Tal-Ezer and Kosloff [6] and developed the acoustical wave propagator (AWP) technique for describing the propagation and scattering of one-dimensional acoustical wave packets. Peng and Pan [7,8] further extended this technique to investigate the time-domain flexural wave propagation in thin plates and dynamic stress concentration on a stepped plate. The aim of the present paper is to apply the AWP technique to analyze the wave propagation and scattering and dynamic stress concentration in a ribbed plate. Dynamic stress concentration factors in the time domain are discussed in detail.

2. Theory of the AWP technique

Plates with rib or beam structures are common components of many practical engineering structures, as shown in Fig. 1. In this paper, investigation of the wave propagation and dynamic stress concentration is based on Mindlin's theory. When disturbed, wave motion occurs in the plate. The wave motion generates dynamic moments and shear forces which result in internal stresses.

The plate is subjected to an external transverse point load $P(x_0, y_0, t)$ that is suddenly applied, as illustrated in Fig. 1. This load can be defined as an initial displacement. Meanwhile, two kinds of moments (bending moments and twisting moments) and the plate transverse shear forces are involved.

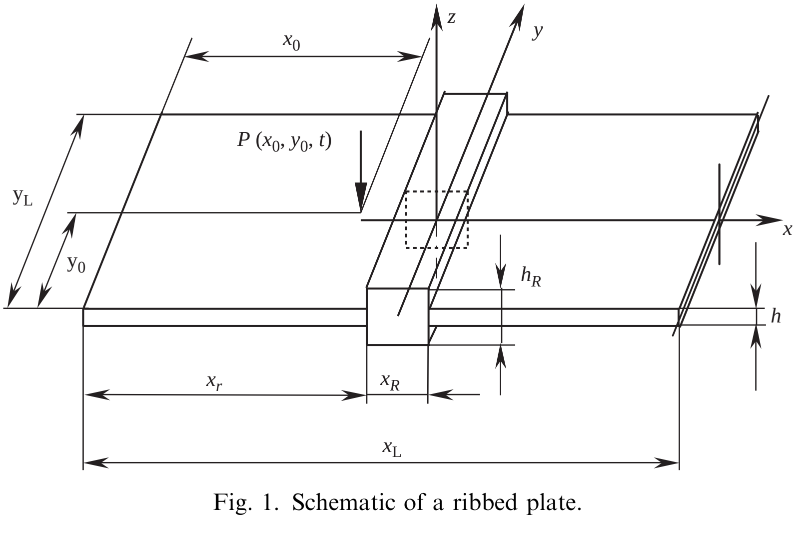

Fig. 1. Schematic of a ribbed plate.

From the stress–strain relations, the stresses are given by [9]

$$\sigma_x = \frac{Ez}{1-\upsilon^2}\left(\frac{\partial \psi_x}{\partial x} + \upsilon \frac{\partial \psi_y}{\partial y}\right), \quad \sigma_y = \frac{Ez}{1-\upsilon^2}\left(\frac{\partial \psi_y}{\partial y} + \upsilon \frac{\partial \psi_x}{\partial x}\right),$$
$$\sigma_{xy} = \frac{Ez}{2(1+\upsilon)}\left(\frac{\partial \psi_x}{\partial x} + \frac{\partial \psi_y}{\partial y}\right), \tag{1}$$

where E is Young's modulus and υ is the Poisson ratio of the plate material. ψ_x and ψ_y are the rotation angles of a line which is normal to the mid-surface before the deformation, about the x- and y-axes, respectively.

The principal stress can be calculated by [10]

$$\sigma_P = \frac{\sigma_x + \sigma_y}{2} + \frac{\sqrt{(\sigma_x - \sigma_y)^2 + 4(\sigma_{xy})^2}}{2}. \tag{2}$$

The derivatives of the moments and shear forces can be obtained as

$$\frac{\partial M_x}{\partial t} = D\left[\frac{\partial \omega_x}{\partial x} + \upsilon \frac{\partial \omega_y}{\partial y}\right], \quad \frac{\partial M_y}{\partial t} = D\left[\frac{\partial \omega_y}{\partial y} + \upsilon \frac{\partial \omega_x}{\partial x}\right],$$
$$\frac{\partial M_{xy}}{\partial t} = D\frac{(1-\upsilon)}{2}\left[\frac{\partial \omega_y}{\partial x} + \frac{\partial \omega_x}{\partial y}\right],$$
$$\frac{\partial Q_x}{\partial t} = \kappa^2 Gh\left(\frac{\partial V}{\partial x} + \omega_x\right), \quad \frac{\partial Q_y}{\partial t} = \kappa^2 Gh\left(\frac{\partial V}{\partial y} + \omega_y\right), \tag{3}$$

where $D = Eh^3(x,y)/(12(1-\upsilon^2))$ is the flexural rigidity of the plate and

$$h = h(x,y) = \begin{cases} h_R, & (x,y) \subseteq RIB, \\ h, & \text{other}, \end{cases}$$

where h_R and h are the thickness of the rib and the plate, respectively. $\omega_x(x,y)$, $\omega_y(x,y)$ and V are, respectively, the angular velocities of the plate and velocity in the z-axis, where $\omega_x = \partial\psi_x/\partial t$, $\omega_y = \partial\psi_y/\partial t$ and $V = \partial W/\partial t$. Q_x and Q_y are the shear forces in the x- and y-axes, respectively; G is the modulus of the rigidity; and κ is a shear factor.

The governing equations of motion of the ribbed plate system are derived as

$$\frac{\partial M_x}{\partial x} + \frac{\partial M_{xy}}{\partial y} - Q_x = \frac{\rho h^3}{12}\frac{\partial^2 \psi_x}{\partial t^2}, \quad \frac{\partial M_{xy}}{\partial x} + \frac{\partial M_y}{\partial y} - Q_y = \frac{\rho h^3}{12}\frac{\partial^2 \psi_y}{\partial t^2},$$
$$\rho h \frac{\partial^2 W}{\partial t^2} = \frac{\partial Q_x}{\partial y} + \frac{\partial Q_y}{\partial x} + P, \tag{4}$$

where ρ is the mass per unit area of the plate.

The system state equation can be obtained by combining Eq. (3) with Eq. (4)

$$\frac{\partial}{\partial t}[\omega_x \quad \omega_y \quad V \quad Q_x \quad Q_y \quad M_x \quad M_y \quad M_{xy}]^{\mathrm{T}}$$
$$= -\hat{\mathbf{H}}[\omega_x \quad \omega_y \quad V \quad Q_x \quad Q_y \quad M_x \quad M_y \quad M_{xy}]^{\mathrm{T}}, \tag{5}$$

where

$$\hat{\mathbf{H}} = \begin{bmatrix} 0 & 0 & 0 & \dfrac{12}{\rho h^3} & 0 & -\dfrac{12}{\rho h^3}\dfrac{\partial}{\partial x} & 0 & -\dfrac{12}{\rho h^3}\dfrac{\partial}{\partial y} \\ 0 & 0 & 0 & 0 & \dfrac{12}{\rho h^3} & 0 & -\dfrac{12}{\rho h^3}\dfrac{\partial}{\partial y} & -\dfrac{12}{\rho h^3}\dfrac{\partial}{\partial x} \\ 0 & 0 & 0 & -\dfrac{1}{\rho h}\dfrac{\partial}{\partial y} & -\dfrac{1}{\rho h}\dfrac{\partial}{\partial x} & 0 & 0 & 0 \\ -\kappa^2 Gh & 0 & -\kappa^2 Gh\dfrac{\partial}{\partial x} & 0 & 0 & 0 & 0 & 0 \\ 0 & -\kappa^2 Gh & -\kappa^2 Gh\dfrac{\partial}{\partial y} & 0 & 0 & 0 & 0 & 0 \\ -D\dfrac{\partial}{\partial x} & -D\upsilon\dfrac{\partial}{\partial y} & 0 & 0 & 0 & 0 & 0 & 0 \\ -D\upsilon\dfrac{\partial}{\partial x} & -D\dfrac{\partial}{\partial y} & 0 & 0 & 0 & 0 & 0 & 0 \\ -\dfrac{D}{2}(1-\upsilon)\dfrac{\partial}{\partial y} & -\dfrac{D}{2}(1-\upsilon)\dfrac{\partial}{\partial x} & 0 & 0 & 0 & 0 & 0 & 0 \end{bmatrix}. \tag{6}$$

Eq. (5) can be rewritten by integrating Eq. (6) with respect to time

$$\phi(x, y, t) = \mathrm{e}^{-(t-t_0)\hat{\mathbf{H}}}\phi(x, y, t_0), \tag{7}$$

where ϕ is a state vector consisting of the angular velocities ω_x and ω_y, velocity V, shear forces Q_x and Q_y, bending moments $M_x(x, y, t)$ and $M_y(x, y, t)$, and one of the twisting moments, $M_{xy}(x, y, t)$, of the plate. $\mathrm{e}^{-(t-t_0)\hat{\mathbf{H}}}$ is defined as the acoustical wave propagator for flexural waves in ribbed plates. The operation of the AWP subjected to the initial state vector $\phi(x, y, t_0)$ is used to evaluate the state vector $\phi(x, y, t)$ of an acoustical wave at any time t. Since the material properties are defined as a function of position, it is worth noting that the effect of boundaries and spatial variation of the acoustical media have been already included in the system operator $\hat{\mathbf{H}}$. In other words, the plate and the rib do not have to be formulated separately, so the AWP technique is more explicit and elegant than other methods.

If the thickness of the rib is smaller than sizes in other dimensions, so the classical Kirchhoff thin plate theory is regarded as a special case of Mindlin plate theory. For this case, Eq. (5) can be simplified into

$$\frac{\partial}{\partial t}\begin{bmatrix} V \\ M_x \\ M_y \\ M_{xy} \end{bmatrix} = -\hat{\mathbf{H}}\begin{bmatrix} V \\ M_x \\ M_y \\ M_{xy} \end{bmatrix}, \tag{8}$$

where

$$\hat{\mathbf{H}} = \begin{bmatrix} 0 & -\dfrac{1}{\rho h}\dfrac{\partial^2}{\partial x^2} & -\dfrac{1}{\rho h}\dfrac{\partial^2}{\partial y^2} & -\dfrac{2}{\rho h}\dfrac{\partial^2}{\partial x \partial y} \\ D\left(\dfrac{\partial^2}{\partial x^2} + \upsilon\dfrac{\partial^2}{\partial y^2}\right) & 0 & 0 & 0 \\ D\left(\dfrac{\partial^2}{\partial y^2} + \upsilon\dfrac{\partial^2}{\partial x^2}\right) & 0 & 0 & 0 \\ D(1-\upsilon)\dfrac{\partial^2}{\partial x \partial y} & 0 & 0 & 0 \end{bmatrix}. \tag{9}$$

3. Numerical scheme of the AWP

3.1. The Chebyshev polynomial expansion and fast Fourier transformation scheme

It is necessary to expand this exponential propagator $e^{-(t-t_0)\hat{\mathbf{H}}}$ in order to evaluate its operation on the initial wave packet. Different expansions of the propagator along with the technique used to calculate the spatial derivatives lead to different time-evolution schemes. Recent work on the time-domain Schrödinger equation shows that the Chebyshev polynomial expansion (CPE) scheme has some distinct features. The main feature is that very long time steps can be used in the calculation; in some cases, a single time step completes the whole calculation. Another feature is that the expansion coefficients of Chebyshev polynomials decay exponentially when the order of the coefficient function is sufficiently larger than its argument. Matrix operator algebra is required for the implementation of the acoustical wave propagator. Since the real Chebyshev polynomials used in the expansion of the acoustical wave propagator are defined in the ranges of $[-1, 1]$, the normalized system operator $\hat{\mathbf{H}}'$ can be calculated by $\hat{\mathbf{H}}' = \hat{\mathbf{H}}/\lambda_{\max}$, where $\lambda_{\max}$ represents the maximum eigenvalue of the system operator $\hat{\mathbf{H}}$.

The acoustical wave propagator is expanded in Chebyshev polynomials of the first kind, and Eq. (7) can be rewritten as

$$\phi(x, y, t) = \sum_{k=0}^{\infty} a_k(R) T_k(\hat{\mathbf{H}}')\, \phi(x, y, t_0), \tag{10}$$

where $a_k(R) = 2I_k(R)$ except $a_0(R) = I_0(R)$ and $I_k(R)$ is the kth order modified Bessel function of the first kind; $R = (t - t_0)\lambda_{\max}$.

The Chebyshev polynomials in Eq. (10) can be calculated by

$$T_0(\hat{\mathbf{H}}') = \mathbf{I}, \quad T_1(\hat{\mathbf{H}}') = \hat{\mathbf{H}}', \quad T_{k+1}(\hat{\mathbf{H}}') = 2\hat{\mathbf{H}}' T_k(\hat{\mathbf{H}}') - T_{k-1}(\hat{\mathbf{H}}') \quad \text{when } k \geqslant 1. \tag{11}$$

If the initial state vector $\phi(x, y, t_0)$ and R are determined, the expansion coefficients can be calculated by the modified Bessel function of the first kind. Thus the AWP operation becomes the calculation of the Chebyshev polynomial $T_k(\hat{\mathbf{H}}')$, which mainly involves the evaluation of spatial derivatives.

Therefore, the following Fourier and inverse Fourier transformations are used to calculate the spatial derivatives of function $\phi(x, y, t)$:

$$\frac{\partial^n}{\partial x^n}\phi(x,y,t) = F^{-1}\{(\mathrm{j}k_x)^n F[\phi(x,y,t)]\} \quad \text{and} \quad \frac{\partial^n}{\partial y^n}\phi(x,y,t) = F^{-1}\{(\mathrm{j}k_y)^n F[\phi(x,y,t)]\}, \tag{12}$$

where $F[\,]$ and $F^{-1}\{\,\}$ represent the Fourier transformation and inverse Fourier transformation, respectively. k_x and k_y are the bending wave numbers in the x- and y-axes, respectively.

Pan et al. [5,7,8] have examined the accuracy of the Fourier transformation method for evaluating spatial derivatives. When the spatial sampling intervals Δx and Δy are given, the discrete Fourier expansion of a wave packet supports the maximum wave number (equivalent to the shortest wavelength or the highest frequency). As mentioned above, R is a function of $\lambda_{\max}$ which is obtained from the system operator $\hat{\mathbf{H}}$ by the equation $(\hat{\mathbf{H}} - \lambda\mathbf{I})\phi = 0$. For example, the normalization factor R related to $\hat{\mathbf{H}}$ in Eq. (9) can be calculated by

$$R = \sqrt{\frac{Eh^2}{12\rho(1-\upsilon^2)}}\left\{\left(\frac{\pi}{\Delta x}\right)^2 + \left(\frac{\pi}{\Delta y}\right)^2\right\}(t - t_0). \tag{13}$$

About the boundary condition, a Gaussian function G_f is introduced to implement the convolution with thickness function $h(x, y)$ and smooth the discontinuity. If very sharp boundaries are present, a large Gaussian factor will be used. Meanwhile, more grid points should be involved to assure the convergence. The effect of the number of grid points on the predicted results will be discussed in the following section.

3.2. Comparison of the predicted results by the AWP technique with the exact analytical solutions

Since the numerical convergence and stability of the Chebyshev–Fourier scheme have been examined in Refs. [5,7,8], in this paper, the predicted results obtained from the AWP technique are compared with the exact analytical solution of the maximum stress in a flat plate. The displacement has the following analytical solution [9]:

$$W(r,t) = \frac{f_0\sigma^4}{(\sigma^4 + b^2t^2)}\mathrm{e}^{[-\sigma^2r^2/4(\sigma^4+b^2t^2)]}\left\{\cos\left(\frac{br^2t}{4(\sigma^4+b^2t^2)}\right) + \frac{bt}{\sigma^2}\sin\left(\frac{br^2t}{4(\sigma^4+b^2t^2)}\right)\right\}, \tag{14}$$

where $b = (Eh^2/(12(1-\upsilon^2)\rho))^{1/2}$; $W(r,t), \sigma$ and f_0 represent the deflection displacement of the plate in the z-axis, Gaussian factor and a constant, respectively.

The first and second order derivatives of $W(r, t)$ are given by

$$\frac{\partial W(r,t)}{\partial r} = \frac{f_0\sigma^2 r}{2(\sigma^4+b^2t^2)^2}\mathrm{e}^{[-\sigma^2r^2/4(\sigma^4+b^2t^2)]}\left\{(b^2t^2-\sigma^4)\cos\left[\frac{br^2t}{4(\sigma^4+b^2t^2)}\right] - 2b\sigma^2 t\sin\left[\frac{br^2t}{4(\sigma^4+b^2t^2)}\right]\right\},$$

$$\frac{\partial^2 W(r,t)}{\partial r^2} = \frac{f_0\sigma^2}{4(\sigma^4+b^2t^2)^3}\mathrm{e}^{[-\sigma^2r^2/4(\sigma^4+b^2t^2)]} \times \left\{\begin{aligned} &(2b^4t^4 - 3b^2\sigma^2r^2t^2 + \sigma^6r^2 - 2\sigma^8)\cos\left[\frac{br^2t}{4(\sigma^4+b^2t^2)}\right] \\ &+ bt(3\sigma^4r^2 - b^2r^2t^2 - 4\sigma^6 - 4b^2\sigma^2t^2)\sin\left[\frac{br^2t}{4(\sigma^4+b^2t^2)}\right]\end{aligned}\right\}. \tag{15}$$

The stresses can be calculated by

$$\sigma_r = -\frac{Eh}{2(1-\upsilon^2)}\left\{\frac{\partial^2 W}{\partial r^2} + \upsilon\frac{1}{r}\frac{\partial W}{\partial r}\right\}, \quad \sigma_\theta = -\frac{Eh}{2(1-\upsilon^2)}\left\{\frac{1}{r}\frac{\partial W}{\partial r} + \upsilon\frac{\partial^2 W}{\partial r^2}\right\}, \quad \tau_{r\theta} = 0. \tag{16}$$

The principal stress is calculated by

$$\sigma_P = \max\{\sigma_r, \sigma_\theta\}. \tag{17}$$

The material used in the calculation of exact analytical solutions is a steel plate. Its material properties are given as follows: $E = 21.6 \times 10^{10}\ \mathrm{N/m^2}$, $\upsilon = 0.3$ and $\rho = 7800\ \mathrm{kg/m^3}$. The dimensions of the plate in the x, y and z directions are 10, 10 and 0.002 m, respectively. The Gaussian factor σ, a constant f_0 and the number of grid points N are, respectively, 0.1, 0.001 and 100. The initial displacement is located at the centre of this plate.

When $t = 0.034$ s, the propagation of the wave packet covers the observation area ($-6\ \mathrm{m} \leqslant x \leqslant 4\ \mathrm{m}$ and $-5\ \mathrm{m} \leqslant y \leqslant 5\ \mathrm{m}$). Fig. 2 shows the comparison of the principal stress between the predictions of the Chebyshev–Fourier scheme and the exact analytical solution. The agreement between the results of the Chebyshev–Fourier scheme and the exact analytical solution is seen to be very satisfactory. Therefore, this scheme can be used to predict accurately the distribution of dynamic stress concentration.

3.3. The effect of the number of grid points on the predicted results

As mentioned above, the number of grid points N has a significant effect on the predicted results. There is a minimum value $N_{\min}$ to assure the convergence of the Chebyshev–Fourier scheme. Fig. 3 shows the predicted results of the principal stress σ_P along $y = 0$ m and at $t = 0.01$ s and different N. When $N < 100$, there are not enough points involved in the calculation, and the accumulation of numerical error impairs the predicted accuracy. In some cases, the calculation becomes dispersion quickly. When $N > 100$, with an increase in N, the accuracy of the predicted

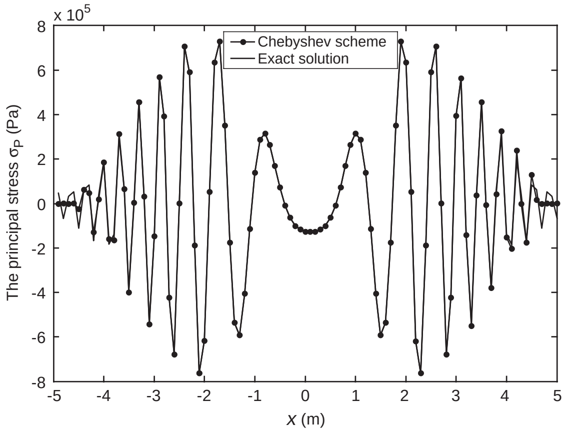

Fig. 2. Comparison between the Chebyshev–Fourier scheme and the exact analytical solution when $y = 0$ m and $t = 0.034$ s.

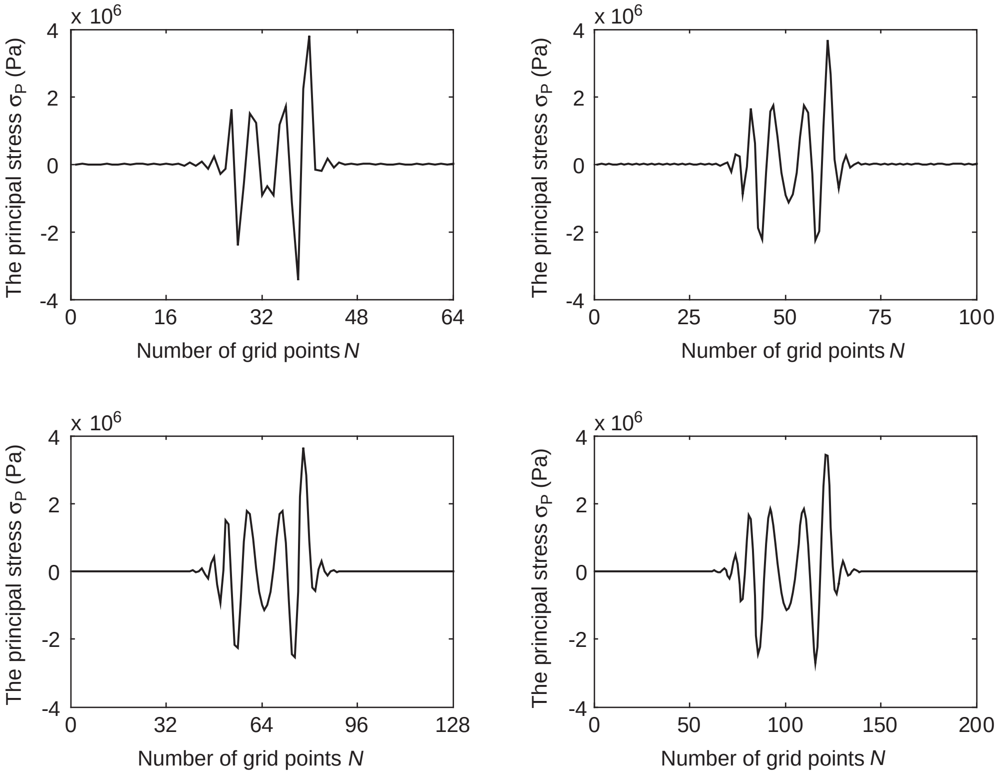

Fig. 3. The predicted results of the principal stress σ_P along $y = 0$ m and $t = 0.01$ s and different N.

results of the principal stresses improves slightly. Therefore, $N_{\min} = 100$ is used to predict the distribution of dynamic stress.

4. Numerical examples and discussion

The same material is used in numerical calculation. Absolute values of parameters are given as follows: $E = 21.6 \times 10^{10}$ N/m^2, $\upsilon = 0.3$, $h = 0.002$ m, $h_R = 0.005$ m, $x_r = 6$ m, $x_R = 0.02$ m, $\rho = 7800$ kg/m^3 and $\sigma = 0.1$, $x_0 = 5$ m and $y_0 = 5$ m, and the dimension of this plate is 10 m × 10 m. The expansion coefficients of Chebyshev polynomials are related to the modified Bessel functions of the first kind.

The following initial state vector is chosen to demonstrate the implementation of AWP on an initial wave packet in a ribbed plate:

$$\phi(x, y, t) = [\,\omega_x(x, y, 0) \quad \omega_y(x, y, 0) \quad 0 \quad Q_x(x, y, 0) \quad Q_y(x, y, 0) \quad M_x(x, y, 0) \quad M_y(x, y, 0) \quad M_{xy}(x, y, 0)\,]^{\mathrm{T}}, \tag{18}$$

where $\omega_x(x,y,0)$, $\omega_y(x,y,0)$, $Q_x(x,y,0)$, $Q_y(x,y,0)$, $M_x(x,y,0)$, $M_y(x,y,0)$ and $M_{xy}(x,y,0)$ are determined by the initial displacement $W(x,y,0) = W_0 \mathrm{e}^{-[(x-x_0)^2+(y-y_0)^2]/4\sigma^2}$ and the material properties. In this simulation, $W_0 = 0.001$ m, the number of grid points N is 100 and the spatial sampling intervals $\Delta x = \Delta y$ are 0.1 m. A plate with infinite length in the x and y dimensions is used, and the spatial range used to observe the evolution of wave packet is $-6\ \mathrm{m} \leqslant x \leqslant 4$ m and $-5\ \mathrm{m} \leqslant y \leqslant 5$ m.

Fatigue failures happen frequently in the regions with high stress concentration, and understanding the distribution of dynamic stress concentration is very useful for engineering design. Complete information of the whole system at any point and any time can be obtained from the above equations. In particular, the principal stress occurring at any point and any time can be calculated. For example, Fig. 4 shows the distribution of the principal dynamic stress σ_P in a ribbed plate at different times. For a given impulse of Gaussian wave packet, at $t = 0$ s, the principal stress is concentrated on a smaller central area. As time increases, stress concentration begins to spread out with decreased magnitude. The most interesting feature in Figs. 4(b) and (c) is the spatial wave interference pattern in the time-domain principal stresses. At a discontinuity, incident bending waves are partly reflected, and the interference between the incident and scattered waves causes constructive and destructive stress zones, as illustrated clearly in Figs. 4(c) and (d). These are analogous to the interference of sound pressure in front of a hard wall surface.

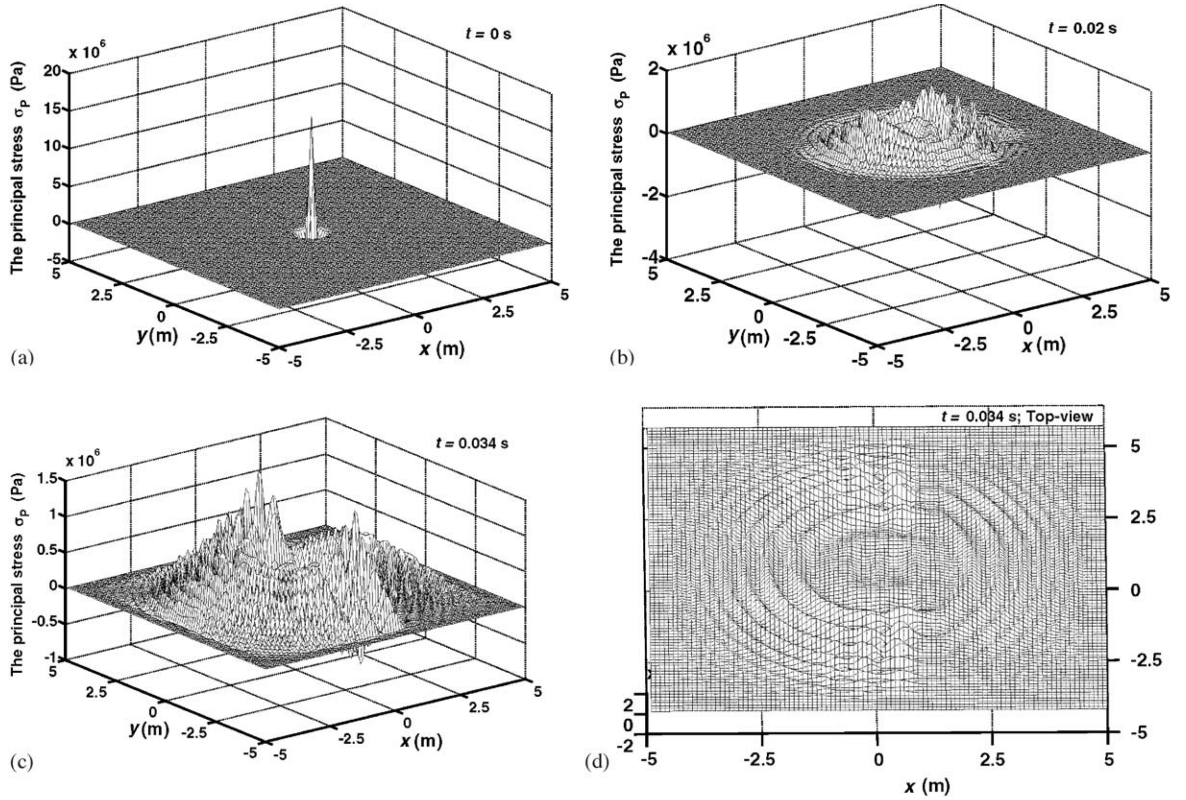

Fig. 4. Distribution of the principal stress σ_P at different times.

When the first incident wave arrives at the rib, the scattered waves are produced and combined with the following incident waves. At $t = 0.02$ s, due to the effect of more scattered waves from the rib, more peaks are focused around the rib. It is noted that, at $t = 0.034$ s, two stress concentration distributions along the rib are shown in Figs. 4(c) and (d). These distributions depend on the thickness ratio of the plate and the rib, the characteristics of plate material, width of the rib, and the distance between impulse point and discontinuity. The results in Fig. 4 agree well with the analysis by Ungar [2] in which the portion of the plate on the incoming near-side of the rib experiences greater maximum stresses and strains in the presence of the rib than if no rib is present.

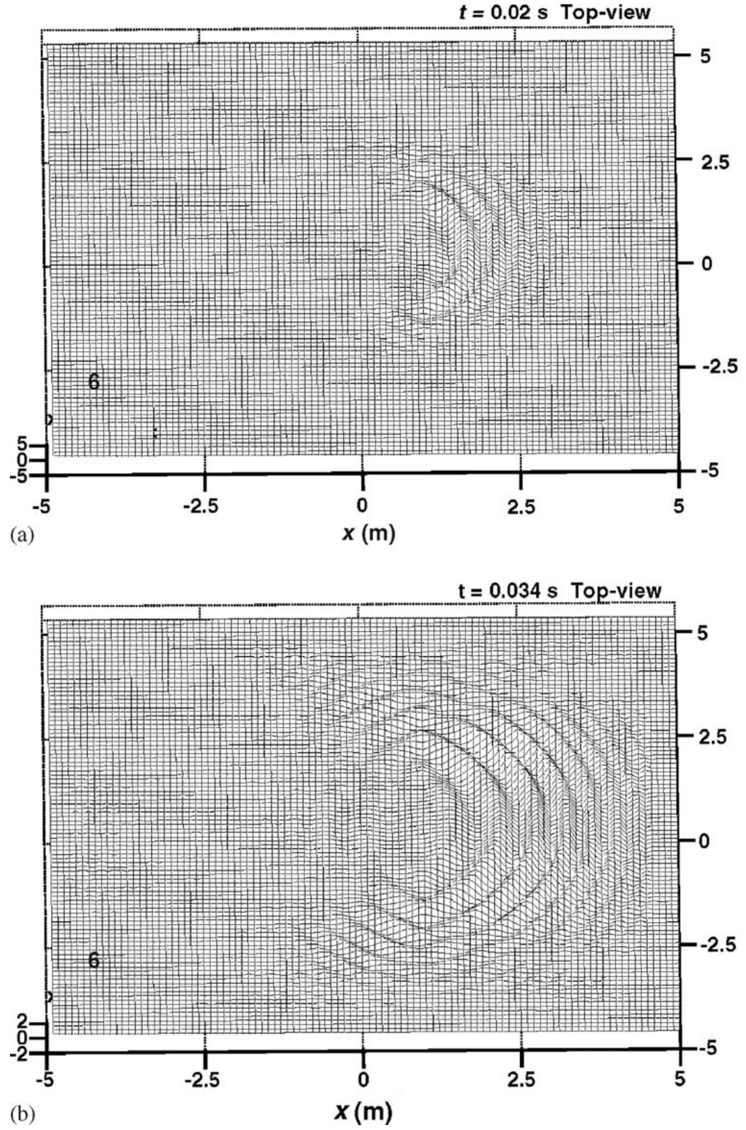

Fig. 5. Distribution of the scattered wave in plate at different times.

Furthermore, to explain the patterns in Fig. 4, the diffracted flexural waves are analyzed and decomposed into two parts: the incident waves in a plate without the rib, and the scattered waves caused by the rib. They are defined by $\phi(x, y, t)_{Di} = \phi(x, y, t)_{Sc} + \phi(x, y, t)_{Di}$, where $\phi(x, y, t)$ represents the state vector in the plate; and subscripts *In*, *Sc* and *Di* represent the incident waves, the scattered waves, and the diffracted flexural waves, respectively. Distribution of the scattered waves is illustrated in Figs. 5. When $t = 0.02$ s, the incident waves reach the rib, and cause scattered waves. At $t = 0.034$ s, another observation from Fig. 5(b) is that more scattered waves spread out and focus on two arcs near the left side of the rib. Similarly, the degree of curve depends on the plate thickness ratios, the material properties of the plate, and the distance between the distributed location and discontinuity. Different from a sphere wave input, the magnitude of each component in the Gaussian wave packet varies with time. As mentioned above, the scattered waves vary with the incident waves, discontinuity condition and material properties. As time increases, the magnitudes and distribution of the diffracted flexural waves will change with the incident waves and scattered waves. Fig. 5 gives a good explanation of the principal stress distribution of distributed flexural waves as shown in Fig. 4. The most interesting feature in Fig. 5(b) is that the spatial wave interference patterns are very different from those obtained in a stepped plate [7]. Fig. 6 shows the distribution of the predicted points.

Due to propagating wave symmetrically about the x-axis, twelve points in the rib are chosen to observe the principal stress σ_P in the time domain, shown in Fig. 7. With the discontinuity, the ratio of the maximum positive/negative value of stress in the plate with the rib to the maximum positive/negative value in the plate without the rib at the same point, is called the stress concentration factor. Fig. 8 shows the dynamic stress concentration factors of twelve points in the

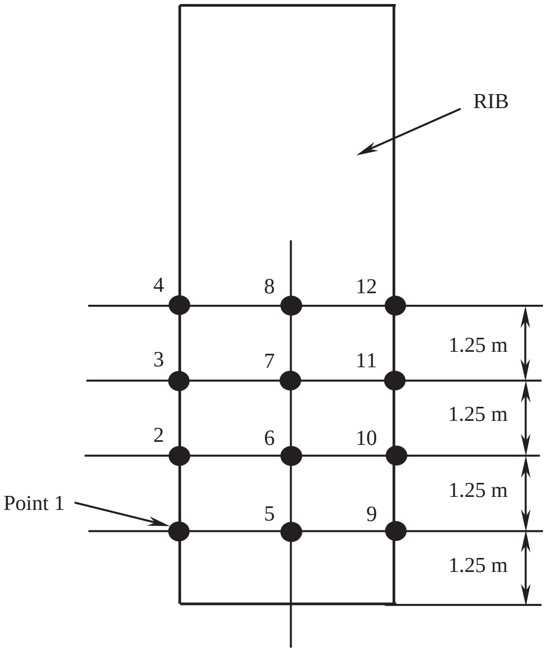

Fig. 6. Schematic of 12 predicted points.

rib. The stress concentration factors at points 2, 4, 8 and 12 have large values. At points 8 and 12, the factors as high as 3 have been illustrated in Fig. 8. Conversely, due to the effect of the interference of the incident waves and scattered waves, the values of dynamic stress concentration

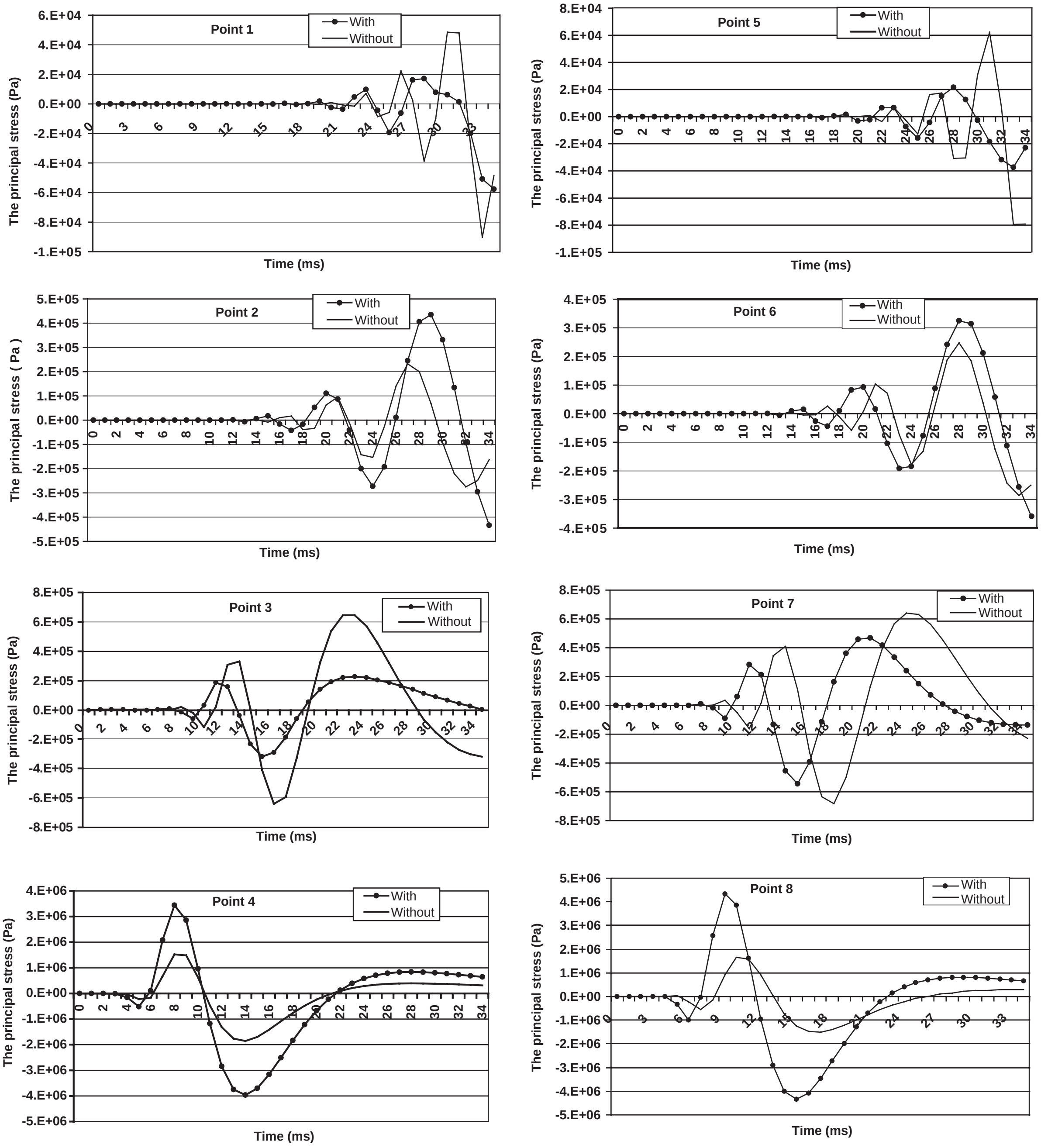

Fig. 7. Dynamic stresses of 12 predicted points.

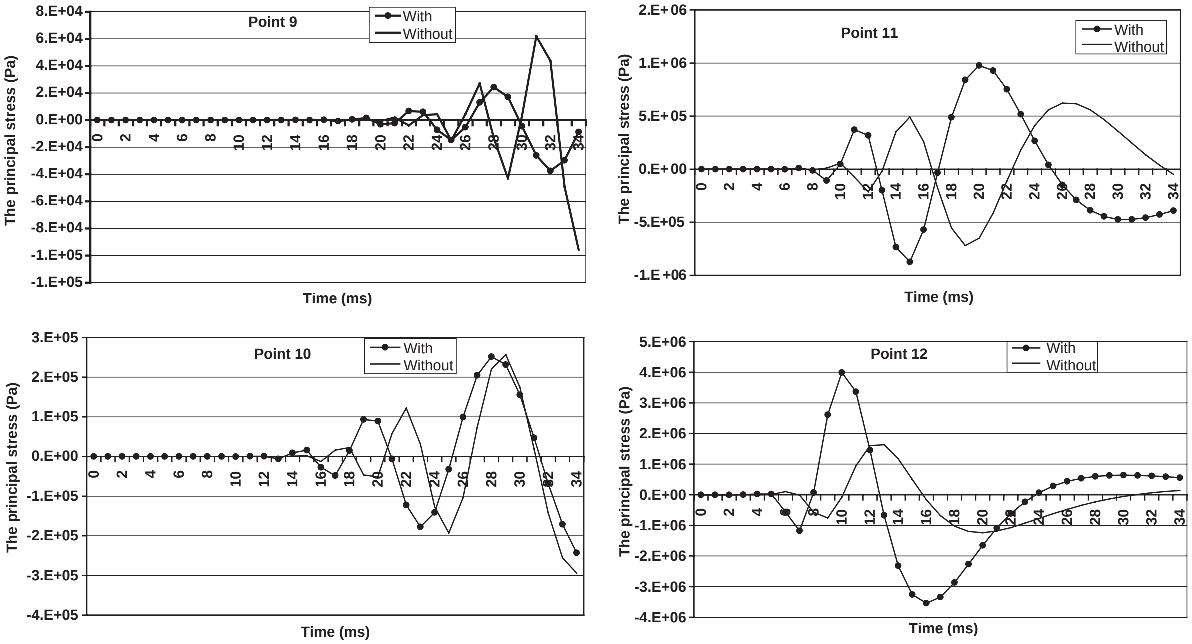

Fig. 7 (*continued*).

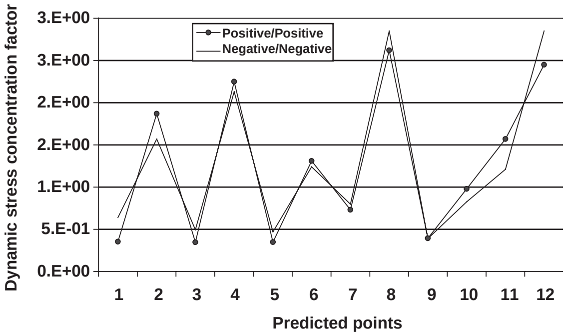

Fig. 8. Dynamic stress concentration factors of 12 predicted points.

factors at points 1, 3, 5, 7 and 9 are less than 1. With the AWP technique, the complete information of the whole system at any point and any time can be easily obtained.

The material properties and damping characteristics of a ribbed plate have significant effects on the displacement, moment and dynamic stress concentration; work in this direction is in progress.

5. Conclusions

In this paper the acoustical wave propagator technique is extended to describe the time-domain evolution of wave packets in a ribbed plate. A Chebyshev polynomial expansion scheme is implemented to carry out the operation of the acoustical wave propagator. Compared with the exact analytical solution, this scheme is found to be accurate and computationally effective for the prediction of the time-domain evolution of acoustical waves. The patterns of the principal stress enable better understanding of the distribution of dynamic stress concentration and pre-fatigue at structural discontinuities.

Acknowledgements

The author wishes to express his gratitude to Professor J. Pan and Dr. J.B. Wang for their assistance in numerical analysis and Margaret Jones for valuable discussion. The author thanks the University of Western Australia for financial support from Australian Postgraduate Research Scholarship and Julian Hunka Scholarship.

References

[1] A. Mukherjee, M. Mukhopadhyan, A review of dynamic behavior of stiffened plates, *The Shock and Vibration Digest* 18 (1986) 3–8.
[2] E.E. Ungar, Transmission of plate flexural waves through reinforcing beams; dynamic stress concentration, *Journal of the Acoustical Society of America* 33 (1961) 633–639.
[3] S.M. Stearn, Spatial vibration of stress, strain and acceleration in structures subject to broad frequency band excitation, *Journal of Sound and Vibration* 12 (1970) 85–97.
[4] S.M. Stearn, The concentration of dynamic stress in a plate at a sharp change of section, *Journal of Sound and Vibration* 15 (1971) 353–367.
[5] J. Pan, J.B. Wang, Acoustical wave propagator, *Journal of the Acoustical Society of America* 108 (2000) 481–487.
[6] Tal-Ezer, R. Kosloff, An accurate and efficient scheme for propagating the time-dependent Schrödinger equation, *Journal of Chemistry and Physics* 15 (1984) 3967–3971.
[7] S.Z. Peng, J. Pan, Acoustical wave propagator technique for time-domain analysis of dynamic stress in a step plate, *Proceedings of SAE International Noise and Vibration Conference*, MI, USA, NVC12, 2003.
[8] S.Z. Peng, J. Pan, Acoustical wave propagator for time-domain flexural waves in thin plates, *Journal of the Acoustical Society of America* 115 (2004) 467–474.
[9] K.M. Morse, K.U. Ingard, *Theoretical Acoustics*, McGraw-Hill, New York, 1968.
[10] W.F. Riley, L.D. Sturges, D.H. Morris, *Mechanics of Materials*, Wiley, New York, 1999.